Unravelling a novel mechanism in polymer self-assemblies: An order-order transition based on molecular interactions between hydrophilic and hydrophobic polymer blocks

* This contribution is dedicated to the late Françoise Winnik

Lukas Hahn[1], Theresa Zorn[2], Josef Kehrein[3], Tobias Kielholz[4], Anna-Lena Ziegler[1], Stefan Forster[1], Benedikt Sochor[5], Ekaterina S. Lisitsyna[6], Nikita A. Durandin[6], Timo Laaksonen,[6,7] Vladimir Aseyev[8], Christoph Sotriffer[3], Maike Windbergs[4], Ann-Christin Pöppler,[2,] and Robert Luxenhofer[1, 8,*]*

[1]Functional Polymer Materials, Chair for Advanced Materials Synthesis, Institute for Functional Materials and Biofabrication, Department of Chemistry and Pharmacy, Julius-Maximilians-University Würzburg, Röntgenring 11, 97070 Würzburg, Germany

[2]Institute of Organic Chemistry, Department of Chemistry and Pharmacy, Julius-Maximilians-University Würzburg, Am Hubland, 97074 Würzburg, Germany

[3]Institute of Pharmacy and Food Chemistry, Department of Chemistry and Pharmacy, Julius-Maximilians-University Würzburg, Am Hubland, 97074 Würzburg, Germany

[4]Institute of Pharmaceutical Technology and Buchmann Institute for Molecular Life Sciences, Goethe University Frankfurt, Max-von-Laue-Str. 15, 60438 Frankfurt am Main, Germany

[5]Chair for X-Ray Microscopy, Julius-Maximilians-University Würzburg, Josef-Martin-Weg 63, 97074 Würzburg, Germany

[6]Faculty of Engineering and Natural Science, Tampere University, Korkeakoulunkatu 8, 33720 Tampere, Finland

[7]Division of Pharmaceutical Biosciences, Faculty of Pharmacy, University of Helsinki, Viikinkaari 5 E, 00014 Helsinki, Finland

[8]Soft Matter Chemistry, Department of Chemistry, and Helsinki Institute of Sustainability Science, Faculty of Science, Helsinki University, 00014 Helsinki, Finland

*correspondence to: robert.luxenhofer@helsinki.fi, ann-christin.poeppler@uni-wuerzburg.de

Keywords: Inverse gelation, poly(2-oxazoline), poly(2-oxazine), aromatic moieties, worm-to-sphere transition

Abstract

Thermoresponsive hydrogel formation upon cooling in aqueous media is rarely described for synthetic polymers in the literature. However, if the sol-gel transition occurs in the physiologically relevant range (0-40 °C), there are many possible applications in areas such as drug delivery and biofabrication. Here, we describe a new mechanism of a thermally induced order-order transition in polymer self-assembly of an ABA triblock consisting of hydrophilic A blocks and a hydrophobic aromatic B block. Small-angle X-ray scattering confirmed worm-to-sphere transition upon heating on the nanoscale level while wide-angle X-ray scattering indicated a more uniform ordering of the macromolecular chains on the scale of 4-7 Å. NMR spectroscopy showed reduced mobility of various polymer segments in the hydrogel state, especially in the hydrophobic aromatic region. More importantly however, solution and solid-state NMR investigations also revealed close proximity of hydrophobic and hydrophilic repeat units in the gel state, which is less pronounced in the sol state. This interaction between the hydrophilic and hydrophobic block is responsible for the order-order transition and –*ipso facto*– inverse thermogelation. This unusual interaction is supported *in silico* by molecular dynamics modeling. Changes in the structure of the hydrophilic A blocks can be used to tune the gel strength, persistence, and gelation kinetics. This order-order transition based on unexpected and previously not described interactions between the hydrophilic and the hydrophobic repeat units opens new avenues to control and design macromolecular self-assembly.

Introduction

Thermoresponsive phase separation of polymer solutions upon heating is an entropic effect and widely discussed in literature.[1] Polymers displaying a lower critical solution temperature (LCST) are structurally diverse and can be found in the families of poly(ether)s, poly(acrylamide)s, poly(2-oxazoline)s and many others. In contrast, examples of UCST (upper critical solution temperature) type phase separation are more rarely found, especially for UCST in purely aqueous media.[2, 3] Such systems are discussed for different applications as smart biomaterials if the transition takes place at or around physiological temperatures and in physiological media. In some cases, physical hydrogel formation (sol-gel transition) can be observed instead of precipitation (coil-globule transition) due to changing aggregation patterns. Block copolymers with thermogelling properties are well-known in literature,[4, 5] with Pluronic® F127 being arguably the most prominent example.[6] Mostly, thermogelation relies on a thermally triggered disorder-order transition from random coils to polymer micelles forming dense colloidal packings.[7] In contrast, Armes and co-workers described a thermogelling system based on an interesting and unusual heating induced worm-to-sphere order-order transition,[8] which could be tuned with respect to the critical gelation temperature.[9] Later, Penfold et al. described a pH- and thermosensitive system that combined pH-responsive vesicle-to-worm transition and thermosensitive worm-to-sphere transition.[10] More recently, a thermoresponsive poly(*N*-(2-hydroxypropyl)methacrylamide)-poly(2-hydroxypropyl)methacrylate) diblock copolymer was described, which formed spheres (4 °C, weakly turbid free flowing fluid), worms (22 °C, turbid free standing gel) or vesicles (50 °C, milky-white free flowing dispersion) in aqueous solution.[11]

Very recently, we described a cooling induced and reversible sphere-to-worm and concurrent sol-gel transition in aqueous solution (Figure 1).[12] A ABA-type block copolymer amphiphile poly(2-methyl-2-oxazoline)-*b*-poly(2-phenyl-2-oxazine)-*b*-poly(2-methyl-2-oxazoline) (pMeOx-*b*-pPheOzi-*b*-pMeOx=A-pPheOzi-A) featuring the novel aromatic PheOzi repeat unit. At 5 °C, the polymer exhibited long interconnected worm-like aggregates, which transformed into small, uniform and spherical polymer micelles upon heating. The temperature, at which the system liquified and its viscosity decreased

several orders of magnitude was 32 °C. While inverse thermoreversible gelation is well known for bio- or bioderived polymers such as agarose or gelatin, there are only few synthetic systems described in the literature.[2] Arguably best known is poly(N-acryloyl glycinamide) (PNAGA), already described by Haas et al. in 1967.[13] Fu and Zhao reported gels that form upon cooling of aqueous solutions of various poly(acrylamide-co-acrylonitrile)-b-poly(poly(ethylene glycol) methyl ether methacrylate)-b-poly(acrylamide-co-acrylonitrile) (P(AAm-co-AN)-b-PPEGMMA-b-P(AAm-co-AN)[14] as well as UCST-type nanogels.[15] In addition, Lele and co-workers described hydrophobically modified copolymers that undergo inverse thermogelation.[16] All these known systems have in common that intermolecular and intramolecular hydrogen bonding between polymer repeat units can occur, which is indeed the main driving force for the UCST phenomenon in general. In stark contrast, A-pPheOzi-A cannot undergo such hydrogen bonding between repeat units and neither pMeOx nor pPheOzi are thermoresponsive *per se*. In addition, we believe A-pPheOzi-A is the first example of a cooling induced sphere-to-worm transition. Therefore, the question is: what is the mechanism of this order-order and concomitant inverse thermogelation? Using a variety of state-of-the-art analytic tools complemented by molecular modeling, we aimed to elucidate the molecular origins of this novel gelation mechanism in detail. We found that the order-order transition in self-assembly is based on a previously undescribed interaction between the hydrophilic MeOx repeat units and the hydrophobic, aromatic PheOzi repeat units, leading to a compaction of the former onto the latter, which in turn leads to the sphere-to-worm morphology transition as the packing parameter increases. Testing this suggested mechanism, variation of the hydrophilic repeat units could be successfully used to tune the gelation behavior.

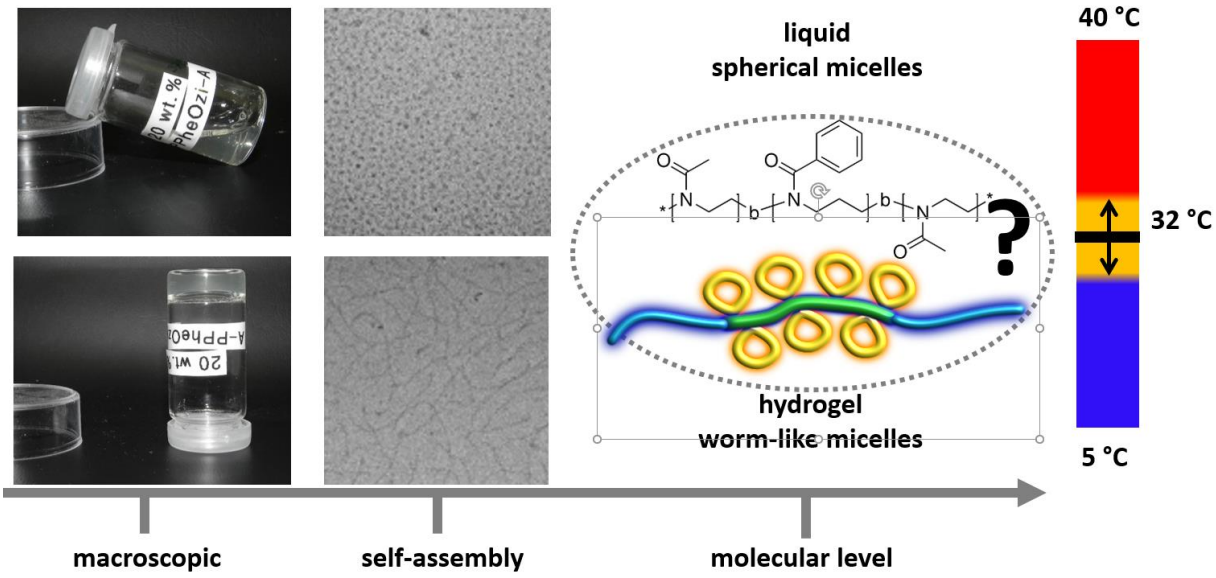

Figure 1| Summary of the study. The polymer amphiphile poly(2-methyl-2-oxazoline)-*b*-poly(2-phenyl-2-oxazine)-*b*-poly(2-methyl-2-oxazoline) (pMeOx-*b*-pPheOzi-*b*-pMeOx = A-PPheOzi-A = A-B-A) showed unique inverse thermogelling properties.[12] In the liquid state, the polymer self-assembled into spherical micelles. Upon cooling an order-order transition into worm-like micelles was observed. (TEM images reprinted with permission from reference [12]). In this study a detailed elucidation of the order-order transition is presented with the focus on polymer interactions on a molecular level. The color code on the right is used throughout this study to highlight the samples macroscopic state.

Materials and Methods

All chemicals and reagents were used from Sigma-Aldrich (Steinheim, Germany) or TCI-chemicals (Eschborn, Germany) and were used as received unless otherwise mentioned. The polymer pMeOx-*b*-pPheOzi-*b*-pMeOx (= A-pPheOzi-A) was prepared and used as described previously.[22] The monomers 2-ethyl-2-oxazoline (EtOx) and 2-methyl-2-oxazine (MeOzi) were synthesized like described by Witte and Seeliger.[17] Deuterated dichloromethane (d_2DCM) and D_2O as NMR solvent were obtained from Deutero GmbH (Kastellaun, Germany). Methyl trifluoromethylsulfonate (MeOTf), EtOx, MeOzi and PheOzi were refluxed over CaH_2 for several hours and distilled under reduced pressure. Benzonitrile (PhCN) was dried over phosphorus pentoxide.

Dynamic light scattering

Dynamic light scattering (DLS) experiments were performed using an ALV CGS-3 multi detection goniometry-system (Langen, Germany) equipped with a He-Ne-laser (632.8 nm) and 8 optical avalanche photodiodes-detector with an angular detector spacing of 16 ° (correlation time 45 s, 3 runs). Scattering angles between 20 ° and 147 ° were measured in 4 angle sets (4x8 detectors) and a 5 ° angle interval for each detector at 15 °C and 40 °C. Prior to each measurement, samples were filtered in dust-free cuvettes using Millex-LG 0.2 µm filters under laminar flow. The polymer concentration was 0.1 g/L (2 mM aqueous $NaNO_3$). All samples were stored at the measurement temperature for 24 h. The decay of the electric field-time autocorrelation function (ACF) was fitted using triexponential fit functions (equation 1) like described previously:[18]

$$g_1(t) = a_1 \cdot e^{\left(-\frac{t}{\tau_1}\right)} + a_2 \cdot e^{\left(-\frac{t}{\tau_2}\right)} + a_3 \cdot e^{\left(-\frac{t}{\tau_3}\right)} \quad (1)$$

with the amplitudes a_i and the decay times $\tau_i = \frac{1}{q^2 \cdot D_i}$, where q is the absolute value of the scattering vector. In the case of polydispersity, the translational diffusion coefficient D was obtained by extrapolation to zero angle and in the limit of high dilution given by

$$\langle D \rangle_z^{-1} = \frac{\sum_i a_i}{\sum_i a_i \cdot D_i^{-1}} \quad (2)$$

Using the Stokes-Einstein equation the (apparent) hydrodynamic radius R_h was obtained by

$$R_h = \frac{k_B \cdot T}{6 \cdot \pi \cdot \eta \cdot D} \quad (3)$$

with k_B being the Boltzmann constant, η is the viscosity of the solvent and T the temperature (15 °C or 40 °C).

Small- and wide-angle X-ray scattering (SAXS, WAXS)

SAXS and WAXS experiments were carried out using an in-house setup, which was built by Fraunhofer EZRT (Fürth, Germany). It consists of a MicroMax-007 HF X-ray source (Rigaku, Japan) and a Eiger R 1M detector unit (Dectris, Switzerland). The sample-detector distance can be varied between 5 cm and 3.5 m, which corresponds to possible Q-values between 0.005 and 5 $Å^{-1}$. The complete setup is operated in a vacuum below 0.1 mbar to reduce air scattering. The sample solutions were placed in quartz capillaries (inner diameter: 1 mm, wall thickness: 10 µm) (Hampton Research, Aliso Viejo, California), which were positioned perpendicularly to the X-ray beam. The presented experiments were done at sample-detector distances of 57 mm, 565 mm and 1560 mm with an integration time of 15 min for the shortest distance and 240 min for the two longer configurations. All distances were calibrated using a silver behenate standard sample. For each sample, data was acquired for different temperatures between 5 °C – 50 °C. To achieve thermal equilibrium, the sample (10 wt.% aqueous solution) was kept at the desired temperature for 15 min prior to each measurement. The SAXS data, which was obtained at the two largest distances, was calibrated in terms of absolute intensities using glassy carbon as a secondary calibration standard.[19, 20] The scattering curves of the hydrogels were obtained by azimuthal integration taking the samples thickness, X-ray transmission, detector accuracy, setup geometry and solvent scattering into account following the standard procedures described in literature.[21]

Temperature dependent nuclear magnetic resonance (NMR) experiments in solution

All experiments in solution were performed at a Bruker Avance III HD 600 spectrometer (Karlsruhe, Germany) operating at 600.4 MHz equipped with a BBFO 5 mm probe using a BCU-02 temperature control unit. ^{1}H NMR experiments of a 20 wt.% A-pPheOzi$_{15}$-A sample in D_2O were acquired with a 30 ° flip angle and 8 or 16 scans without sample spinning. A series of variable temperature experiments

was performed in the range from 2 °C to 39.15 °C in a step size of 3 to 5 °C. The sample was kept at the desired temperature for 10 minutes prior to each measurement. Temperature calibration was done using 4 % MeOH in MeOD and 80 % ethylene glycol in DMSO-d_6. All recorded spectra were referenced using the temperature dependent HDO signal. For quantitative characterization of the temperature induced phase transition the fraction p was calculated with the integrals $I(T)$ and $I(T_0)$ at the respective temperatures T and T_0 using the following equation:[22]

$$p = 1 - \frac{I(T)}{I(T_0) * \frac{T_0}{T}} \tag{3}$$

The highest signal intensity was measured at 39.15 °C (T_0). Reductions of signal intensities are indicated by $p < 0$. 2D ^{1}H-^{1}H nuclear Overhauser effect NMR spectroscopy (NOESY) experiments at 5 °C and 40 °C were recorded using the noesygpphpp pulse sequence (scans: 32, t_1 increments: 256, relaxation delay: 2.5 s). To ensure discrimination between cross-relaxation and spin-diffusion different mixing times (40 µs, 60 µs, 80 µs, 150 µs and 250 µs) were used. For better visualization of the aromatic region, phase and baseline correction of 2D data was confined to the range of 6-8 ppm and TDeff was set to 2867 in the f2 dimension. Additionally, 1D slices of relevant aromatic regions were extracted. ^{1}H spin-lattice relaxation times T1 were measured with the inversion recovery pulse sequence t1ir at 5 °C and 40 °C. For measuring the T1 relaxation times of HDO a variable delay from 1-50 s in 12 steps was used with a relaxation delay of 50.0 s. T1 relaxation times of polymer signals were recorded with a variable delay from 0.001-5.0 s in 16 steps and a relaxation delay of 5.0 s. The normalized decay curves for different polymer segments and the HDO signal were fitted using monoexponential fit functions.

Solid-state nuclear magnetic resonance

Solid-state NMR (ssNMR) measurements were performed using a 4 mm double-channel Bruker probe at 9.4 T using between 3 and 5.3 kHz magic angle spinning (MAS). The hydrogel sample was cooled to 273 K prior to measurement. For the ^{13}C CP MAS experiment, a 2 ms ramp (50 to 100 %) on the ^{1}H channel was used during the cross-polarization (CP) contact time for all samples. ^{13}C NMR spectra with direct excitation were recorded with short interscan delays of 1 s to probe mobile components. For

heteronuclear decoupling during acquisition, SPINAL64 was employed with a 100 kHz nutation frequency (^{1}H). The chemical shifts were referenced using adamantane (left signal at 38.48 ppm) by subsequent adjustment of the magnetic field.

Raman spectroscopy

The Raman spectra were recorded on an alpha 300R$^+$ confocal Raman microscope from WITec GmbH (Ulm, Germany) equipped with a 50x objective (NA 0.8, Epiplan Neofluar, Zeiss, Germany) and a 532 nm laser (39.4 mW). A 20 wt.% sample was measured after equilibration at 5 °C and 40 °C using a temperature controllable Peltier stage (LTS 120, Linkam Scientific Instruments Ltd., Tadworth, UK). Spectra are shown as average spectrum of 3 spectra at different locations on the same sample, which were recorded with an integration time of 5 s and 10 accumulations. The resulting data were processed with cosmic ray removal and background subtraction. The bulk water signals at 3100 cm^{-1} - 3700 cm^{-1} were fitted using a Gaussian deconvolution method as described elsewhere.[23, 24]

Fluorescence spectroscopy

The amphiphilic fluorescence probe 2-(4-(dimethylamino)styryl)-1-methylpyridinium iodide (Daspmi) was purchased from Molecular Probes Inc., Life Technologies. The hydrophobic probe 4,4´-difluoro-4-bora-3a,4a-diaza-s-indacene meso-substituted with para-dodecylphenyl (BPC12) was synthesized like described in previous studies.[25] Gibco™ Dulbecco's phosphate-buffered saline (DPBS) pH 7.25 was purchased from Thermo Fisher Scientific (Massachusetts, USA). The steady-state fluorescence spectra of Daspmi (5 µM) and BPC12 (5 µM) in aqueous sol and gel samples at a polymer concentration of 20 wt.% were recorded at different temperatures on a FLS-1000 spectrofluorometer (Edinburgh Instruments, UK) equipped with a thermocontrolled cuvette holder ($\lambda_{exc.}$(Daspmi): 460 nm, $\lambda_{exc.}$(BPC12): 490 nm) comparing the wavelength shift of emission maximum. Fluorescence intensity decay curves were obtained using a time-correlated single photon counting (TCSPC) system (PicoQuant GmbH) equipped with a temperature controlling cuvette holder using quartz cuvettes as described earlier ($\lambda_{exc.}$: 483 nm, cutoff filter > 490 nm).[26] Monitoring wavelengths were 580 nm for Daspmi and 520 nm for BPC12. The fluorescence decays were deconvoluted with the instrumental response to give

the fluorescence lifetime with a resolution of approximately 100 ps. The obtained lifetimes were used for calculating microviscosity values at different temperatures (5 °C, 12 °C, 22 °C and 37 °C) using following equation:

$$\log \tau_f = \log \frac{z}{k_r} + \alpha \log \eta \quad (4)$$

where τ_f is the fluorescence lifetime of Daspmi or BPC12[32] in the solution of a known viscosity η , k_r is the radiative rate constant, and z and α are constants. The linear part of the log τ_f as a function of $\log \eta$ plot was taken as a calibration function to calculate microviscosity values (Figure S3). The viscosities of different water/glycerol mixtures (80-100 wt.% of glycerol) at different temperatures were determined using a LOVIS 2000M rolling ball microviscosimeter from Anton Paar (Graz, Austria) with a LOVIS 1.8 capillary and a steel ball of 1.5 mm diameter. Prior to viscosity measurements, the density of the sample at the specific temperature was recorded using a DMA 4100M density meter from Anton Paar (Graz, Austria). For the corresponding lifetime measurements a concentration of 5 µM of Daspmi and BPC12 were used.

Micro calorimetry (µCAL)

Micro calorimetry measurements were conducted with a Malvern MicroCal PEAQ-DSC microcalorimeter. The heat of the sample was measured relative to pure water and the enthalpy values were normalized to the molar concentration of the aromatic repeat units. After complete dissolution, the samples were stored in the refrigerator at 4 °C for about 48 h, degassed at 5 °C, transferred to the instrument precooled at 2 °C or 10 °C, and kept at the temperature for different times, as indicated, prior to heating. Each sample was heated with the rate of 1 °C/min to 100 °C, after which they were cooled again to the starting temperature with the same rate.

Molecular modeling

We modeled a system containing eight Me-pMeOx$_{35}$-*b*-pPheOzi$_{15}$-*b*-pMeOx$_{35}$-EIP polymers (Me = methyl group, EIP = ethyl isonipecotate), in which the hydrophobic pPheOzi blocks faced each other to

form a single inner strand along the Z axis and the hydrophilic pMeOx blocks were bent outwards. Four individual molecules made up the strand and were subsequently duplicated and moved next to the original polymers along the Z axis, ultimately resulting in two layers of polymers in our simulation box. The stretched out, hydrophilic pMeOx blocks were subjected to an energy minimization and a short, 50 ps long simulation with the Noisé-Poincaré-Andersen method[27, 28] (applying the Amber14:EHT force field[29, 30] with the R-field implicit solvation model[31]) to yield a more compact starting conformation, while keeping the inner strand in a straight orientation. Figure S6A depicts the prepared structure. All modeling was performed with MOE (Molecular Operating Environment 2019.01).[32] The setup was inspired by previous modeling studies regarding worm-like micelles of small molecules, in which the generation of a continuous micelle was also achieved via initial placement of hydrophobic parts in the inner and hydrophilic moieties in the outer regions of the threadlike structure, which was aligned along one axis of the simulation box.[33-35] RESP partial charges[36] of single monomers used as building blocks were derived from calculations with Gaussian 09 Rev. C.01[37] (Hartree-Fock level of theory, 6-31G* basis set); parameters based on the Amber14ffSB[29] and GAFF2[38] force fields were assigned via antechamber and parmchk2 of AmberTools18.[39] During charge derivation monomer structures were capped with residues of the same type (except for the terminal groups, Me-MeOx and EIP, which were capped with a MeOx monomer). The calculated parameters were used to generate a polymer with an initial straight conformation using tleap.[39]

Subsequent solvation of the starting structure with TIP3P water[40] in a simulation box with a minimum border-to-polymer distance of 20 Å in the X and Y directions resulted in a system size of approximately 16 x 18 x 10 nm^3 with 76,730 solvent molecules. Water molecules found inside the inner hydrophobic strand after this initial placement were removed if the distance to the pPheOzi blocks was less than 10 Å. Periodic boundary conditions with minimum image convention were applied during the simulation, which allowed for an infinitely sized worm-like micelle along the Z axis and ensured a sufficient distance between polymers of neighboring boxes along the X and Y dimensions. The simulation was performed using NAMD 2.13[41] with 2 fs time steps. An initial energy minimization of 10,000 steps was conducted before slowly heating the system from 100 K to 278 K over the course of 500 ps. Harmonic constraints

were initially applied on all polymers and gradually reduced over an additional 1.6 ns, allowing a rapid reordering of solvent molecules around the polymers. Langevin dynamics and the Nosé-Hoover Langevin piston method (1 atm) were used for temperature and pressure control in an NPT ensemble. After another 2 ns of equilibration, the production run was performed for 600 ns. Semi-isotropic coupling allowed for fluctuations along the Z axis, independent from the X and Y axes. The particle mesh Ewald method[42] with a cutoff of 1.2 nm was applied and coordinates were saved every 10 ps. Subsequent analyses were performed using cpptraj[43] and images were generated with VMD 1.9.3[44] and PyMOL 2.4.1.[45] Average densities for polymer groups around PheOzi monomers were retrieved as follows: All PheOzi residues were iteratively aligned onto the same monomer. Next, binned occupancy histograms of different moieties around the center of the aligned residue were calculated for the last 100 ns using the grid command in cpptraj. This was performed on a 1.6 x 1.6 x 1.6 nm^3 grid with a 1 Å resolution. After this procedure, the obtained values around each PheOzi monomer were added up at each grid element and divided by the number of analyzed frames (10,000) and monomers (104). Thus, densities represent the average amount of atoms of interest found at each grid element per frame around a single monomer. The first and last PheOzi monomer of each pPheOzi block (16 out of 120) were excluded from this calculation, as these are always situated near the neighboring MeOx residues. Additionally, we analyzed several distances between these PheOzi monomers and the other polymer residues, as well as the angle ω between the plane of nearby amide (N-(C=O)-C) groups and the phenyl ring plane for every 10 ps of the last 100 ns.

Rheology

All experiments were performed using an Anton Paar (Ostfildern, Germany) Physica MCR 301 system utilizing a plate-plate geometry (25 mm diameter) equipped with a solvent trap and Peltier element for temperature adjustment. All aqueous 15 wt.% samples were dissolved at room temperature stirring constantly and incubated at 5 °C for 48 h. In addition, pictures were taken to visualize the gels. A temperature-sweep was performed in oscillation mode from 5-50 °C (heating rate: 0.05 °C/s) using

a fixed amplitude of 0.1 % and angular frequency of 10 rad/s. The long-time gelation experiment at 5 °C was performed at an amplitude of 0.1 % and an angular frequency of 10 rad/s for several hours.

Polymer synthesis

To investigate the influence of the hydrophilic block on the gelation mechanism the polymers Me-pEtOx$_{35}$-*b*-pPheOzi$_{15}$-*b*-pEtOx$_{35}$-EIP and Me-pMeOzi$_{35}$-*b*-pPheOzi$_{15}$-*b*-pMeOzi$_{35}$-PipBoc were synthesized as described several times using MeOTf as initiator and ethyl isonipecotate (EIP) or 1-Boc-piperazine (PipBoc) as terminating agent, respectively.[12] (Detailed characterization of the novel ABA type amphiphiles in SI).

For standard analytics of the synthesized polymer, NMR spectra were recorder on a Bruker Fourier 300 (^{1}H: 300.12 MHz) spectrometer at 298 K from Bruker BioSpin (Rheinstetten, Germany) and calibrated using the solvent signal of d_2DCM.

Gel permeation chromatography

Gel permeation chromatography (GPC) was performed on a Polymer Standard Service PSS (Mainz, Germany) system. Specifications: pump mod. 1260 infinity, MDS RI-detector mod. 1260 infinity (Agilent Technologies, Santa Clara, California, USA), precolumn: 50 x 8 mm PSS PFG linear M; 2 columns: 300 x 8 mm PSS PFG linear M (particle size 7 µm; pore size 0.1 – 1.000 kg/mol) with hexafluoroisopropanol (HFIP, containing 3 g/L potassium trifluoroacetate (KTFA)) as eluent calibrated with PEG standards (molar masses from 0.1 kg/mol to 1000 kg/mol). The columns were held at 40 °C and the flow rate was set to 0.7 mL/min. Dried polymer powders were dissolved in eluent and filtered through 0.2 µm PTFE filters (Rotilabo, Karlsruhe, Germany).

Differential Scanning Calorimetry (DSC)

All measurements were performed using aluminum crucibles on a calibrated DS 204 F1 Phoenix system from NETZSCH (Selb, Germany) equipped with a CC200 F1 controller unit from -50 °C to 200 °C with

three heating and two cooling phases and a cooling rate of 10 °C/min. The third heating cycle was used to analyze the glass transition temperature of dried polymer powders.

Transmission electron microscopy

For transmission electron microscopy (TEM) experiments, the polymers were dissolved in DI water to a final concentration of 20 g L^{-1} and stored at room temperature. 400 mesh copper–rhodium grids (maxtaform) with a homemade carbon layer were glow discharged in air for 1.5 min at medium power in a Harrick PDC-002 plasma cleaner. The 20 g L^{-1} sample was diluted (1/125 or 1/625) and 8 µL were incubated on the grids for 1 min before blotting (Whatman filter paper No. 50). The grids were washed with water (three times) and 2% w/v uranyl acetate (three times). After the last dose of uranyl acetate was applied, the grid was left to incubate for 5 minutes before blotting. A single-tilt room temperature holder in an FEI Tecnai G2 Spirit TWIN transmission electron microscope equipped with a tungsten emitter at 120 kV was used. Images were recorded with an Eagle CCD camera under low-dose conditions. The micrographs were binned two times resulting in a pixel size of 2.2 Å per pixel at specimen level.

Results and Discussion

As previously evidenced by *cryo*TEM investigations, the amphiphile pMeOx-*b*-pPheOzi-*b*-pMeOx reversibly forms worm-like micelles in aqueous media upon cooling.[12] However, these images were recorded at dilute, non-gelling concentrations (c_{gel} ≈ 5 wt.%). To confirm that this order-order transition also occurs at higher concentrations, we conducted temperature dependent small-angle X-ray scattering (SAXS) at above c_{gel} (10 wt.%).

The intensity I as a function of Q from the SAXS measurements was plotted for different temperatures. In the hydrogel state (5 °C), a pronounced structure peak (supporting information, Figure 2A, blue) is followed by two clearly defined regions with different slopes at intermediate and high Q-values, which can be assigned to different self-assembled species. Using a power-law expression[46], the different

slopes can be determined, indicating the presence of spherical micelles and worm-like micelles in the gel state. Above T_{gel}, the worm-like micelles disappear, confirming that the order-order transition found at low concentration also occurs at higher concentration. In addition, the structure peak is shifted towards higher Q-values indicating a lower particle/particle distance in the sol state due to the formation of small spherical micelles (supporting information, Figure 2A, vertical lines). This is a logical consequence of the disintegration of relatively few worm-micelles into much more numerous spherical micelles. The extrapolation of the absolute intensity I to Q_0 (supporting information, Figure S1, horizontal lines) was used as a measure for relative mean particle size, corroborating once more larger particles in gel state (worm-like micelles) in comparison to the sol state (spherical micelles). The qualitative analysis of the SAXS scattering profiles is summarized in more detail in the supporting information (Table S1).

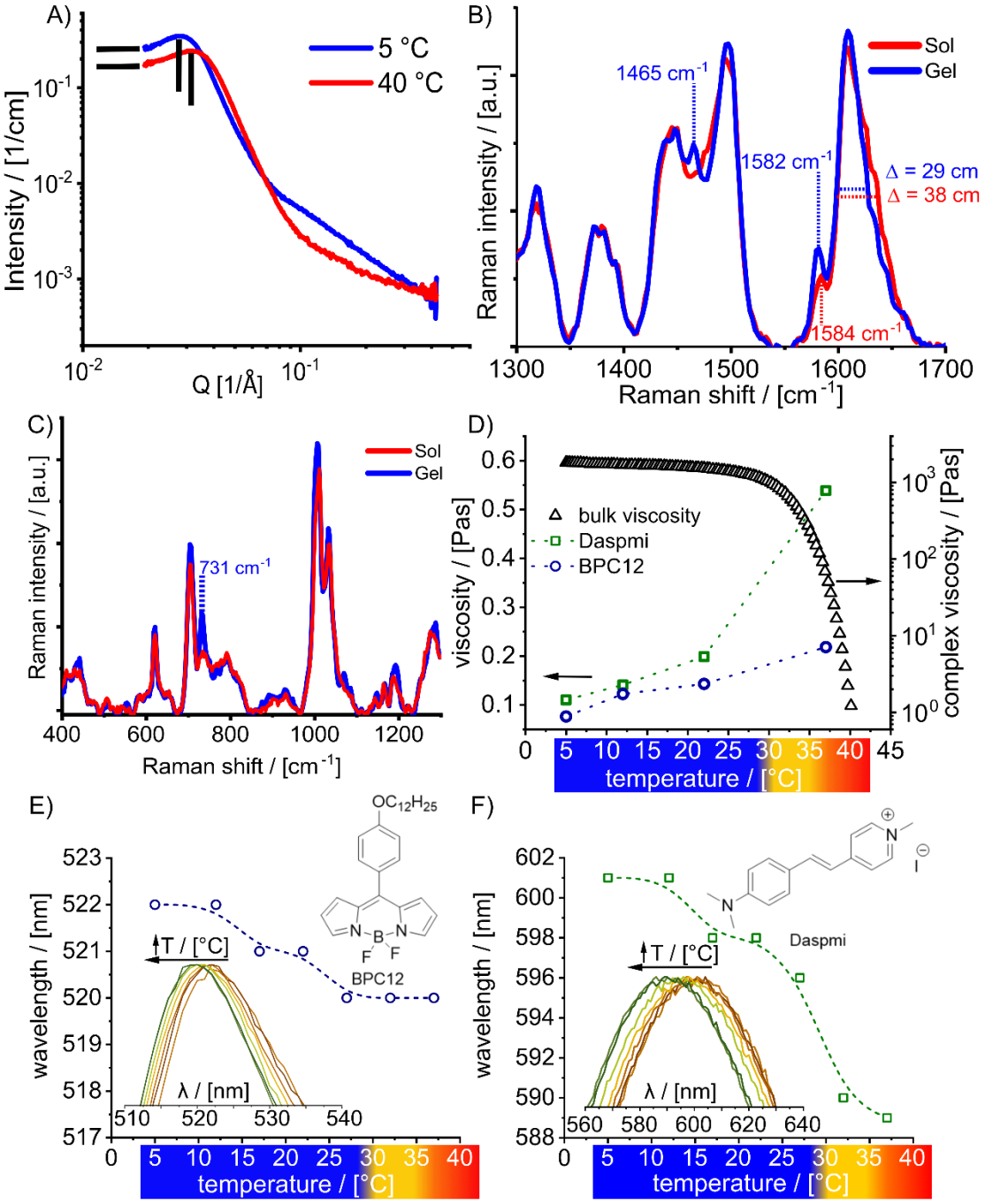

Figure 2| SAXS analysis, microviscosity, and polarity change of aqueous pMeOx-*b*-pPheOzi-*b*-pMeOx solutions. A) SAXS scattering curves at 5 °C (blue, hydrogel) and 40 °C (red, liquid) at 100 g/L. Two defined slopes regions can be defined (triangles). Further, the position of the structure (vertical lines) and absolute intensity of Q →0 (horizontal lines) are different at 5 °C and 40 °C. B) Microviscosity values for Daspmi and BPC12 molecular rotors in a 20 wt.% aqueous polymer sample in fluorescence lifetime experiments as a function of temperature. Bulk viscosity of a 20 wt.% hydrogel was added for comparison using the data obtained in previous studies via oscillatory rheology experiments.[12] Wavelength shift of BPC12 (C) and Daspmi (D) fluorescence emission in steady-state experiments as a function of temperature. In addition, the chemical structure of BPC12 and Daspmi are shown. The color code for the temperature represents the macroscopic state of the sample as described in Figure 1.

Additionally, temperature-dependent wide angle X-ray scattering (WAXS) (Figure S1) provides insights into intra- and interpolymer interactions as previously described for biopolymers[47] and thermogelling

peptides[48]. In the gel state (5 °C, blue), a rather defined peak centered around 4.2 Å was observed, which could be interpreted to hint towards π-π interactions of the phenyl moieties.[49] With increasing temperature, the peak position was maintained, but a noticeable broadening between 4.2 Å and 7 Å indicates reduced order and increased degrees of freedom. From a self-assembly point of view, a transition from spherical to worm-like assembly must correlate with a change in the volume fraction of the hydrophilic to the hydrophobic compartment. Specifically, the relative volume of the hydrophilic compartment has to decrease or the volume of the hydrophobic compartment has to increase upon cooling for a sphere-to-worm transition to occur. If the peak in the WAXS scattering curve corresponds to the hydrophobic compartment, it would suggest rather a decrease in volume due to denser packing. This is a first hint that the molecular origins of the order-order transition do not lie in the hydrophobic compartment (alone) and are not connected to π-π stacking as might be assumed.

Infrared and Raman spectroscopy can provide functional group-selective information on non-covalent polymer interactions, conformations and self-assembly. Overall, the Raman spectra for the dried polymer powder, polymer hydrogel (20 wt.%, 5 °C) and polymer sol (20 wt.%, 40 °C) are quite similar (Figure S2A), but some distinct changes hint at differences in the polymer-polymer interactions between sol and gel state. At 1464 cm^{-1}, a small but clearly distinguishable peak is exclusively observed in the gel (Figure 2B). Unfortunately, both aromatic ring vibrations as well as CH_3 and CH_2 deformation vibrations ubiquitous in the polymer backbone and hydrophilic sidechain appear in this region, making an unambiguous assignment challenging.

The maximum amide band at 1608 cm^{-1} does not shift, but the signal has a slightly higher intensity in the gel state. In addition, the full width-half maximum decreases rather significantly by 25 % from 38 cm^{-1} to 29 cm^{-1}. Similarly, a peak at around 1580 cm^{-1}, which is attributed to the phenyl ring of the hydrophobic repeat units shows increased intensity, becomes more defined, and in addition shifts slightly to lower wave numbers from 1584 cm^{-1} (sol) to 1582 cm^{-1} (gel) (Figure 2B). Albeit in a different system (graphene interaction with polystyrene), such a shift has been attributed to electron donation into the aromatic system as observed in π-π stacking.[50] These observations support the observations

made in WAXS, where a more narrow peak also indicates better defined molecular interactions. In addition, we observed one major differences in the fingerprint region of the Raman spectra. In the gel state, a sharp and moderately intense signal is observed at 731 cm^{-1}, which is much weaker and barely resolved in the sol state. In this spectral region, we expect C-C stretching modes, which are abundant in our polymers. At this point, we cannot hypothesize on the assignment of this signal without further understanding of the system, but will return later to this assignment.

A clear difference between sol and gel state is also observed in the OH region of 3100 cm^{-1} to 3600 cm^{-1}, originating from water molecules. The different types of bonding modes in water molecules can be categorized using Gaussian deconvolution to divide the OH region into areas with different binding strength.[23, 51, 52] Our data suggest that water is less mobile in the hydrogel compared to the sol (Figure S2B) as indicated by the increased contribution of the peak at 3250 cm^{-1} (Figure S2B, red line, 1).

However, arguably more interesting are the changes in macromolecular mobility with the change in self-assembly. Viscosity sensitive fluorescent probes, namely molecular rotors such as 4,4´-difluoro-4-bora-3a,4a-diaza-s-indacene *meso*-substituted with *para*-dodecylphenyl, BODIPY-C12 (BPC12) and 2-(4-(dimethylamino)styryl)-1-methylpyridinium iodide, Daspmi have been used in this context.[26] The fluorescence lifetime of a molecular rotor is affected by the ability to rotate its structural segments with respect to each other, which in turn is strongly dependent on the immediate molecular environment. However, it has to be kept in mind that it is not always clear what this immediate molecular environment is. Here, microviscosities in the sol and gel states were determined by fluorescence lifetime data after appropriate calibration (Figure S3)[53] at four temperatures (5 °C, 12 °C, 22 °C and 37 °C). We intended to probe the temperature-dependent microviscosity of the hydrophobic and the hydrophilic compartment of the self-assemblies by using two different rotors, one being more hydrophobic (BPC12) and the other being more hydrophilic/amphiphilic (Daspmi). Interestingly, in contrast to bulk viscosity (macroviscosity) of the polymer, which is obviously higher in gel state, higher microviscosities were obtained in the sol state and the hydrophilic probe gave almost three times higher values than the hydrophobic one (Figure 2 D). The microviscosities decreased upon gelation and

were similar for both probes below 25 °C. This suggests, albeit indirectly, a more profound change in the hydrophilic compartment upon gelation. Steady-state fluorescence spectroscopy complements the picture. Fluorescence intensity and λ_{max} shift can provide information on polarity changes of the probe´s microenvironment.[54] For both probes, a two-step bathochromic shift was observed at low temperature, indicating an increase in the polarity of the probe microenvironment upon gelation (Figure 2 E,F). This increase supports the suggestion that the probes can be partially expelled from polymeric self-assemblies and become more exposed to polar aqueous solvent. Interestingly, the first polarity change is at a temperature between 12 °C and 17 °C. Again, the change was much more pronounced for Daspmi. Ultimately, the time-resolved and steady-state fluorescence measurements clearly show that the microenvironment of both molecular rotors is more polar and less viscous in the gel state, suggesting that the gelation causes a probe migration out of the condensed polymeric assembly closer to the polymer-water interface. However, this remains indirect evidence.

NMR spectroscopy is a versatile tool to further study the underlying molecular interactions of the order-order transition due to its more straightforward assignability of signals to specific moieties and sensitivity to short-range order phenomena. Therefore, we recorded ^{1}H NMR spectra of a 20 wt.% polymer sample at different temperatures between 2 °C and 39 °C (40 °C). In a first step, all signals in the ^{1}H NMR spectra were assigned (Figure 3 A,B). Notably, the aromatic protons in the sidechain of the hydrophobic polymer block show a broad signal at 6.6-7.6 ppm (signal 5), which differs significantly in appearance between sol and gel state (Figure 3B). Four signal areas around 6.9 ppm, 7.2 ppm, 7.4 ppm and 7.5 ppm (signals 5.1-5.4) can be distinguished. In the hydrogel state (2 °C - 31 °C), an overall low signal intensity with a relatively defined peak at 7.5 ppm and a broad shoulder around 7.4 ppm is observed. Increasing the temperature above the sol-gel transition (34 °C - 40 °C) results in significantly increased signal intensities and reduced line widths suggesting a significant mobility increase for the polymer chains, including the aliphatic region (backbone and CH_3 group of MeOx, signals 1-4). The p-ratio (equation (3)) allows a more quantitative assessment of the relative decrease of the respective peak areas, or the mobility of the associated polymer segments (Figure 3C).

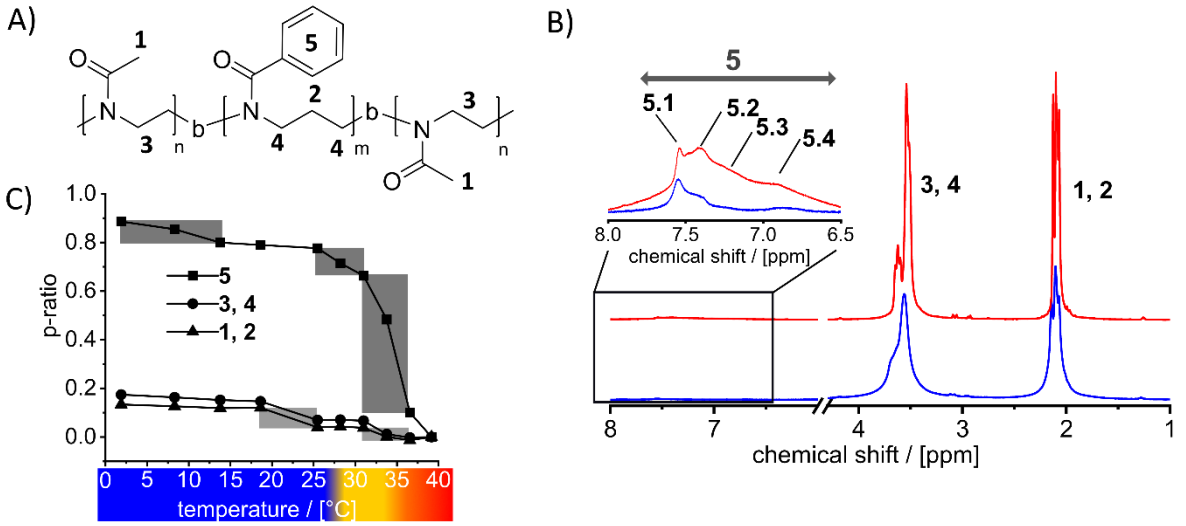

Figure 3| ^{1}H NMR experiments of a 20 wt.% sample in D_2O recorded at different temperatures. A) Structure of the amphiphilic ABA type triblock copolymer pMeOx-*b*-pPheOzi-*b*-pMeOx including numbering scheme. B) ^{1}H NMR spectra at 2 °C (blue) and 39.15 °C (red) of a pMeOx-*b*-pPheOzi-*b*-pMeOx sample alongside signal assignment. C) Calculated *p*-ratio for the intensities of different polymer protons as a function of temperature. The color code for the temperature represents the macroscopic state of the sample as described in Figure 1.

Clearly, the aromatic protons yield the highest p-ratio in the gel-state. Upon heating and coinciding with gel liquefaction, the p-ratio decreases drastically indicating a much more flexible and mobile hydrophobic compartment for the spherical micelles, which is in line with the WAXS data and in clear contrast to the fluorescence probe microviscosities. This strongly suggests that the molecular interactions in the hydrophobic compartment change significantly at or around T_{gel}. At lower temperature, more pronounced hydrophobic or π-π interactions lead to an improved packing and lower mobility. In addition, two minor steps where the p-ratio decreases are observed between 2 °C and 15 °C as well as 25 °C and 30 °C, which will be discussed below. Overall, the hydrophilic block and the backbone appear less affected by the transition corroborating results by Weberskirch et al. and Černoch et al. describing thermoresponsive POx-based homo- and copolymers.[22, 55] However, also for the MeOx units a change in p-ratio is observed at 17-25 °C, followed by a plateau region (20-30 °C), before it drops to zero upon liquefaction. Interestingly, these steps agree with steps observed in steady state fluorescence. Mobility information for the different moieties can also be obtained through the comparison of ^{1}H longitudinal relaxation times T1, which were determined for the sol and gel state, respectively (Figure S4, Table S2). The fact that all polymer segments yield the same trend of decreasing T1-values upon increasing temperature supports the assumption that all parts of the

polymer act in concert in the aggregation process. In contrast, higher T1 values for water in the sol state indicates more mobile water molecules compared to the gel state, corroborating Raman spectroscopy and steady state fluorescence results discussed earlier.

To obtain more insights into the spatial proximity between different moieties in the polymer, 2D ^{1}H-^{1}H NOESY NMR experiments were performed in the gel (5 °C) and sol (40 °C) state (Figure 4). 1D horizontal slices are also shown for better visibility. Stronger NOE signals are visible in the hydrogel state (Figure 4, left, blue) compared to the sol (Figure 4, right, red), which agrees with the hypothesized reduced mobility and data from WAXS (Figure 2A).

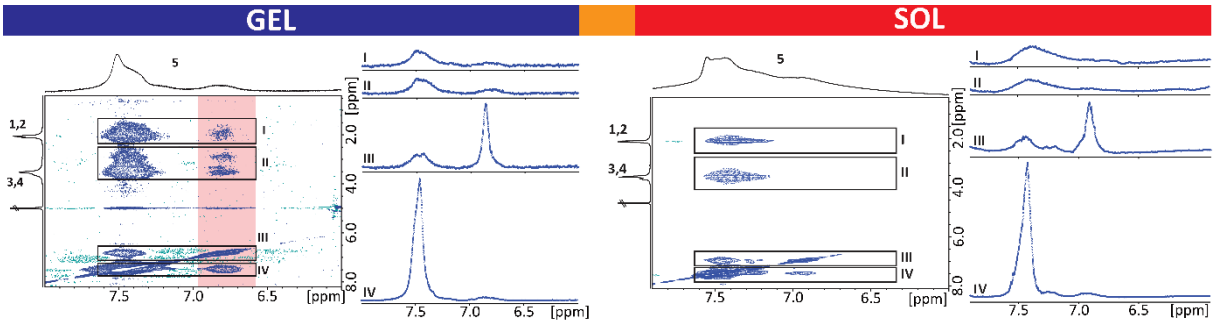

Figure 4| ^{1}H-^{1}H NOESY NMR experiments of a 20 wt.% sample in D_2O recorded with a mixing time of 40 µs. 5 °C (blue, gel state, worm like micelle). 40 °C (red, sol state, spherical micelle). For signal areas of interest 1D slices were extracted and the assignment in figure 6 for the specific polymer signals was used.

Notably, in the sol and gel state, an intense NOE cross peak originating from the aromatic peak at 7.5 ppm can be correlated to the backbone and MeOx sidechain protons. However, in the gel state an additional second cross peak of the aromatic region at 6.9 ppm with the backbone and MeOx sidechain protons is evident despite the overall lower ^{1}H signal intensity in this area compared to the sol state (red square, Figure 4). The observation of an additional NOE signal and, therefore, increased spatial proximity of aromatic and hydrophilic units is a first, but crucial hint at a possible molecular mechanism to explain the unique assembly of this amphiphile into worm-like micelles at lower temperature. If the hydrophilic blocks interact with the hydrophobic block in any significant manner upon cooling, this could reduce the hydrophilic/hydrophobic volume ratio and lead to the observed sphere-to-worm transition. Due to its sensitivity to subtle changes in intermolecular interactions and packing on the

molecular level, solid-state NMR is a versatile tool to improve our understanding of the potential contacts identified so far.

Considering their nature as viscoelastic solids, hydrogels can generally characterized using solid-state NMR experiments.[56] For shear thinning hydrogels such as the present system, one has to consider the possibility that magic angle spinning (MAS) can exert sufficient force to alter the samples properties, e.g. causing liquefaction. Here, ^{1}H NMR experiments at different MAS frequencies (3-5.3 kHz) showed no significant differences (Figure S5). Two different ^{13}C NMR spectra were recorded either through direct excitation (DE) with short interscan delay (1 s) showing predominantly mobile carbon environments (Figure 5A, grey spectrum), while ^{1}H-^{13}C cross polarization (CP) MAS experiments with a contact time of 2 ms reveal more rigid molecular entities due to their dependence on dipolar interactions (Figure 5A, black spectrum). In the spectrum obtained through DE, only signals that can be attributed to MeOx units were visible. No aromatic signals were observed, corroborating once more the reduced mobility of the latter. In the ^{13}C CP MAS NMR spectrum significantly more and broader peaks as well as spinning sidebands (Figure 5A, asterisks in grey spectrum) were observed with phenyl moieties now clearly observable. A MAS rate of 5 kHz or higher is required to avoid substantial overlap between the carbonyl signal of the amide group and the phenyl spinning sidebands. The broader signal (compared to DE spectra) of the amide carbonyl is shifted slightly to smaller ppm values (orange arrow) and additional signals are visible at higher ppm values originating from the phenyl carbonyl groups. Most interesting, however, are two additional signals that are observed in the aliphatic region of the spectrum (red arrows). The signal at 38 ppm is close to the other backbone signals indicating a similar chemical environment, while another new and broad signal appears at 24 ppm adjacent to the signal of the methyl sidechain of the hydrophilic polymer block. In other words, there are two different MeOx populations, one quite mobile and one significantly less mobile.

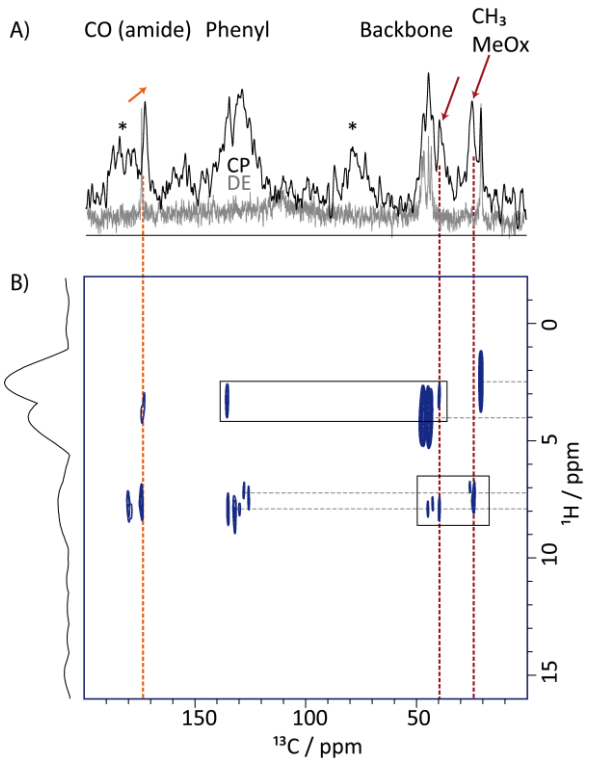

Figure 5| Solid state NMR experiments of a 20 wt.% hydrogel sample. A) Overlay of the ^{13}C NMR spectra recorded at 9.4 T and 5.3 kHz MAS using DE and short interscan delay of 1 s (grey) or CP MAS with 2 ms contact time (black). Spinning sidebands are indicated by asterisks. B) ^{1}H-^{13}C HETCOR MAS spectrum recorded at 9.4 T and a MAS rate of 5 kHz using a contact time of 2 ms. 122 t_1 FID increments were acquired using a recycle delay of 2 s, each with 240 co-added transients. The corresponding ^{13}C NMR spectra are shown at the bottom. Direct CH contacts are indicated by dotted grey lines.

To better understand the nature of these new signals and investigate proximities through space in more detail, a 2D ^{1}H-^{13}C HETCOR experiment with a contact time of 2 ms was recorded (Figure 5B). Due to the relatively long contact time, intra- and intermolecular proximities can be observed in the 2D spectrum as cross peaks. The ^{1}H chemical shifts of the CH_3 groups of MeOx, the backbone, and the two major phenyl environments are indicated by grey dotted, horizontal lines. The three signals highlighted in Figure 5A are indicated by dotted, vertical lines. For the carbonyl signal, cross peaks both in the aromatic and aliphatic backbone region are observed, but due to the polymer structure we cannot know whether the proximity is intramolecular or intermolecular. Furthermore, cross peaks between some of the backbone CH_2 signals and the phenyl signal at higher ppm are also visible (black boxes). Considering the larger intramolecular distance between the backbone and the phenyl ring, this interaction is most likely through space. For the remaining carbon signals in the aliphatic region, it is clear that interactions must occur through space. The more rigid CH_3 group of MeOx at 24 ppm only

visible in the CP-MAS experiment is in a different polymer block than the phenyl moiety. Therefore, the cross peak at 24 / 7.2 ppm can only be explained by ^{1}H-^{13}C proximity through space (< 4 Å) between the hydrophilic and the hydrophobic block. In contrast, the more mobile CH_3 group of MeOx at slightly lower ppm values does not show any cross peaks in the 2D correlation and thus represents the hydrated hydrophilic corona. With this, we can finally formulate a mechanism for the order-order transition and inverse thermogelation in aqueous solutions of pMeOx-b-pPheOzi-b-pMeOx. Our results show that this thermogelation is due to an unexpected interaction between repeat units in the hydrophilic pMeOx blocks and those in the aromatic hydrophobic pPheOzi block. This reduces the volume of the hydrophilic compartment allowing the order-order sphere-to-worm transition. Polymers that show UCST-type thermotransition typically exhibit H-bonding between polymer repeat units, however, this is not possible in the present case. When starting to investigate this mechanism our first hypothesis was that this transition could be linked to π-π stacking within the hydrophobic compartment, but this hypothesis had to be abandoned quickly. A look into the literature yields two other, we believe more probable candidates, the overlap of the lone electron pairs of the amide carbonyl and the aromatic LUMO: $n_{Am} \rightarrow \pi^*_{Ar}$ or interactions of the π-orbitals of the amide and phenyl ring: $\pi_{Am} \bullet\bullet\bullet \pi_{Ar}$. In general, non-covalent n→π* interactions have been described to contribute to the thermostability of the proline-rich protein collagen.[57] Interestingly, proline is the only proteinogenic amino acid that forms tertiary amides akin to the amide groups in POx and POzi. In addition, and even more closely related to the present system, $n \rightarrow \pi^*_{Ar}$ interactions have been described to contribute to the structure formation in peptoids[58], which also contain tertiary amides.

The analytically rather elusive $n \rightarrow \pi^*_{Ar}$ interactions are typically verified by crystallographic data or computational modeling. While the former can be ruled out for our system, we performed an all-atom molecular dynamics (MD) simulation of a single worm-like micelle consisting of full length $pMeOx_{35}$-*b*-$pPheOzi_{15}$-*b*-$pMeOx_{35}$ amphiphiles at 5 °C (Figure S7A). We modeled the pPheOzi blocks as a central inner strand, which is surrounded by the corresponding pMeOx blocks stretching out into the solvent (water). Throughout the 600 ns simulation a single worm-like strand of pPheOzi blocks is preserved.

More interestingly however, the peripheral MeOx repeat units approach the initially solvent-exposed hydrophobic repeat units (Figure 6 A,B), clearly corroborating our model of a hydrophilic shell condensing onto the hydrophobic core.

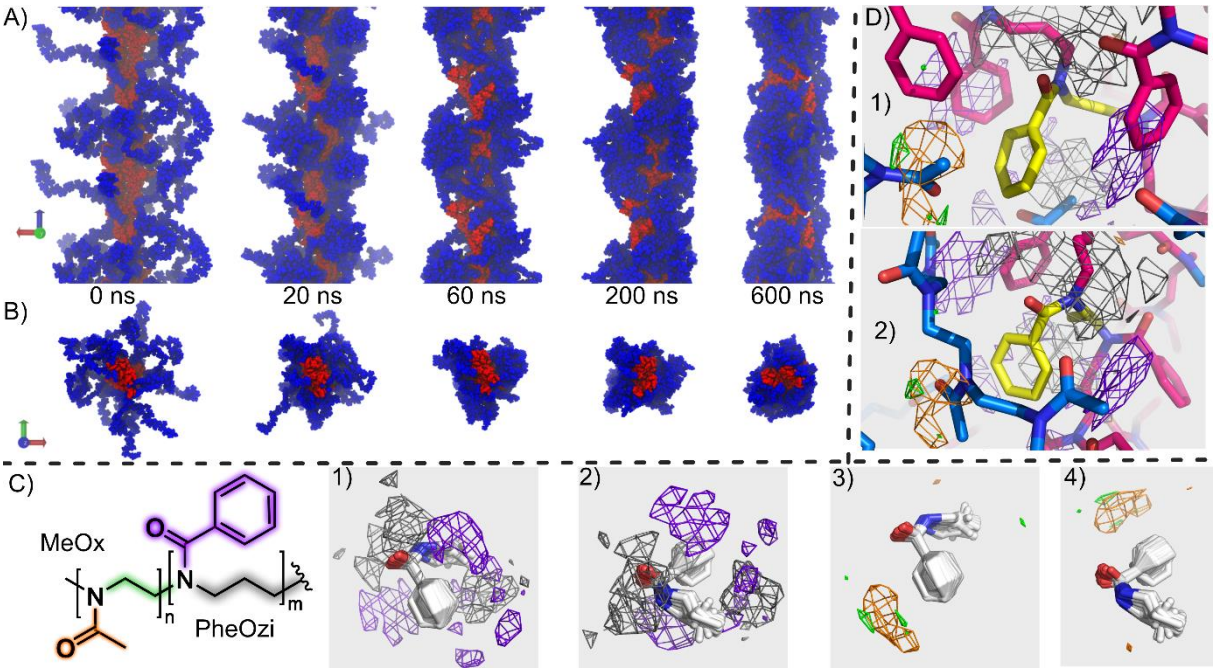

Figure 6| Results of molecular modeling of a worm-like micelle comprising pMeOx-*b*-pPheOzi-*b*-pMeOx amphiphiles. A) Simulation snapshots showing PheOzi monomers as red and MeOx monomers as blue VDW spheres. The simulation box and about half of each neighboring image along the Z axis are illustrated, without solvent molecules depicted. B) Same illustration as seen in A) from an orthogonal perspective (along the Z axis). C) Occupancy density analysis around aligned PheOzi residues (white sticks), showing hotspots for different polymer structures as meshes from two different perspectives. In C-1/2 the violet density represents PheOzi sidechains and the grey density PheOzi backbone atoms (isovalues: 0.08). The two structures on the right in C-3/4 depict densities (isovalues: 0.03) for MeOx backbone atoms (green) and sidechain atoms (orange) from two different perspectives. D) Two example snapshots D-1 and D-2, in which residues at the surface of the micelle overlap with occupancy hot spots depicted in C). pMeOx residues are shown with blue carbon atoms, pPheOzi residues with magenta carbon atoms and the aligned monomer of interest is highlighted in yellow. Densities are shown analogously to C).

Consequently, the radius of gyration of the self-assemblies decreases quickly and reaches a narrow fluctuation range after about 40 ns (Figure S7B, left). While the overall structure becomes clearly more compact, not all pMeOx repeat units come into close contact with pPheOzi residues *in silico*, which in turn are also not completely shielded from the solvent at the end of the simulation, corroborating the observations made in solution NMR spectroscopy. *In silico*, about 53 % of all pMeOx repeat units keep a minimum average distance of more than 5 Å to the pPheOzi blocks over the last 100 ns (including hydrogen atoms for calculation). These would be attributed to the pMeOx repeat units, which were

found more mobile in the ^{13}C DE MAS NMR spectra and which did not show cross peaks with the aromatic rings of pPheOzi in the ^{1}H-^{13}C HETCOR spectrum. We analyzed the solvent-accessible surface area of all pPheOzi units and noticed that this value is mostly decreasing early in the simulation for the aromatic sidechains, indicating that pMeOx monomers are preferably shielding these moieties against water molecules (Figure S7B, middle). The amount of water within 5 Å around polymer residues also decreases quickly, especially for the pMeOx monomers (Figure S7B, right).

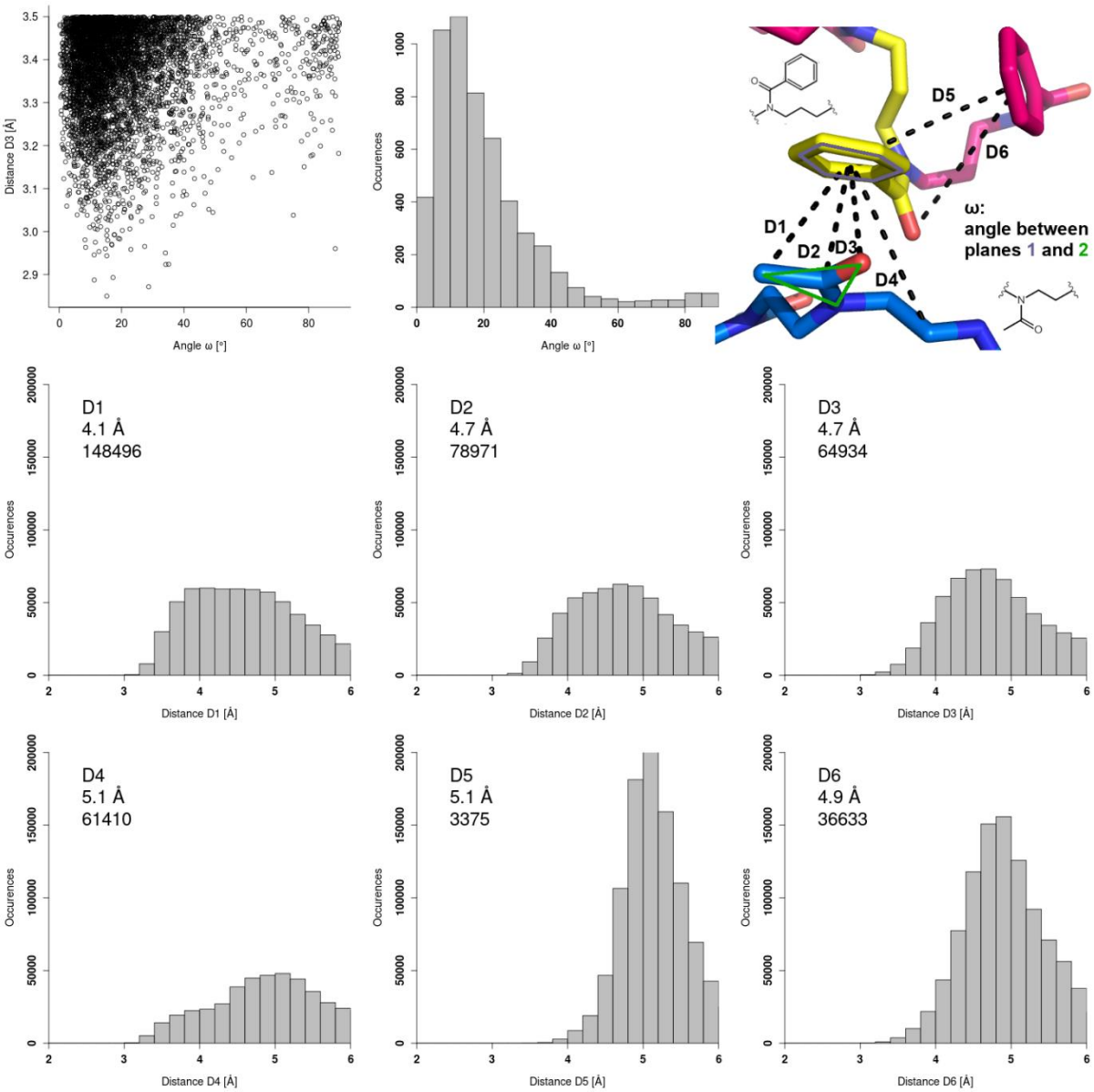

Figure 7| Distribution of computationally derived distances and angles between the amide group and the pheny ring centroid. Histograms for all distances up to 6 Å between PheOzi moieties and the nearest polymer atoms (excluding hydrogen atoms). An illustration describing the distances and the angle ω is given in the top right. Plots show the total amount of occurrences for all snapshots of all 104 pPheOzi residues which were used for density calculation. Numbers in the top left of each histogram illustrate the maximum bin value below 6 Å (bin size: 0.2 Å), as well as the sum of all occurrences between 0 and 4 Å. Additionally, the plot in the top left

shows measurements of the angle ω for all pMeOx carbonyl oxygen atoms which are located nearer than 3.8 Å to the ring centroid (corresponding to distance D3). A histogram for this angle is depicted in the middle of the top row, with a 5 ° bin size.

An illustration of the average occupancy densities of polymer moieties around pPheOzi moieties supports this observation (Figure 6B). The methyl sidechains (of the hydrophilic pMeOx repeat units) are predominantly located close to the aromatic ring of PheOzi sidechains in close proximity to the PheOzi carbonyl group. In contrast, aromatic rings can be found below or above other PheOzi amide groups and near the phenyl ring in the volume which is turned away from the carbonyl group. The pPheOzi backbone atoms are mainly surrounded by other PheOzi residues, only a small fraction of the aromatic repeat units remains solvent-exposed: 17 out of 120 pPheOzi repeat units show an average minimum distance of over 3 Å to any pMeOx in the last 100 ns (taking hydrogen atoms into account). These could be interpreted as sticky patches, which help to mechanically connect different worm-like micelles, adding to the remarkably high storage modulus of the gels.[12] The evidence of such sticky contacts in worm-like micelles was recently discussed by Thurn and Hoffmann.[59] However, we cannot completely rule out that these patches result (in part) from an insufficient number of polymers in our model, as the exact composition of the micelle was not available as input *a priori* from experimental data. For the PheOzi residues analyzed during density calculation, we measured distances to the nearest polymer moieties, as well as the angle ω between the planes of nearby N-(C=O)-C amide groups and the aromatic ring (Figure 7). Distances D1 – D4 reflect the orange and green densities in Figure 6C. A notable number of distances D1 – D3 below 4 Å can be found, highlighting potential interactions between the MeOx sidechains and the phenyl ring. Overall, distances show distributions similar to the results of our WAXS experiments. The distance to the ring centroid is the lowest for the methyl group, while the backbone is situated further away. These measurements support hydrophobic interactions between the phenyl rings of pPheOzi and the methyl sidechain of MeOx repeat units as seen in NMR experiments. With regard to the MeOx carbonyl groups, $n_{Am} \rightarrow \pi^*_{Ar}$ or $\pi_{Am} \bullet\bullet\bullet \pi_{Ar}$ interactions may be hypothesized. While it should be mentioned that the existence of specific interactions between lone pairs and aromatic systems was recently challenged[63] and that the ability of

classical force fields for capturing these can certainly be questioned, occurrences of an angle ω ≤ 90 ° in combination with a distance lower than 3.8 Å of the carbonyl oxygen to the ring centroid are in accordance with previously published measurements for potential $n_{Am}\rightarrow\pi^*_{Ar}$ interactions, e.g. in peptoids.[58, 60] We retrieved very low values for ω with a median of about 19 ° with the above mentioned distance cutoff, indicating suitable conformations for $n_{Am}\rightarrow\pi^*_{Ar}$ or $\pi_{Am}\bullet\bullet\bullet\pi_{Ar}$ interactions. Exemplary simulation snapshots which overlap with the described densities illustrate the interactions between MeOx and PheOzi sidechains (Figure 6D). While some MeOx carbonyl groups showed conformations perpendicular to the ring plane (example D-1), in most cases the amide moiety is placed nearly parallel to the phenyl ring (example D-2). Accordingly, the additional stretching mode at 731 cm^{-1} in the Raman spectra in the gel state should correspond to a C-C bond which is weakened compared to the sol state. We believe that this could be attributed to the C-C bond in the MeOx side chain, which, as the amide interacts with the phenyl ring is weakened, leads to an increased Raman shift.

In summary, the MD simulation conclusively supports our extensive analytical data, in particular those obtained by WAXS and NMR spectroscopy, and the formulated mechanism of the hydrophilic MeOx interacting with the hydrophobic repeat units. This results in a notable condensation of the hydrophilic corona and, thus, enables the worm-to-sphere transition upon cooling. This process may be driven by pMeOx sidechains mainly interacting with aromatic systems of the pPheOzi blocks via hydrophobic, as well as possible $\pi_{Am}\bullet\bullet\bullet\pi_{Ar}$ and $n_{Am}\rightarrow\pi^*_{Ar}$ interactions.

We know from previous studies that small changes in the hydrophobic core prevent worm formation and thermogelation. Specifically, when pPheOzi is exchanged with poly(2-phenyl-2-oxazoline), poly(2-phenyl-2-oxazine) or poly(2-benzyl-2-oxazoline), the resulting ABA triblock copolymers form only spherical micelles and low viscous liquids in water irrespective of the temperature.[12] In contrast, ABA triblock featuring poly(2-phenethyl-2-oxazoline) or poly(2-benzhydryl-2-oxazoline)s from gels but do not undergo any order-order transition but remain spherical micelles.[61, 62] Having derived this novel mechanism behind the order-order transition, we should expect that different hydrophilic blocks affect

the order-order transition and thermogelation. To do so, ABA triblocks featuring slightly different hydrophilic blocks A, poly(2-methyl-2-oxazine) (pMeOzi) and poly(2-ethyl-2-oxazoline) (pEtOx) were prepared (see Table S3, Figure S7).

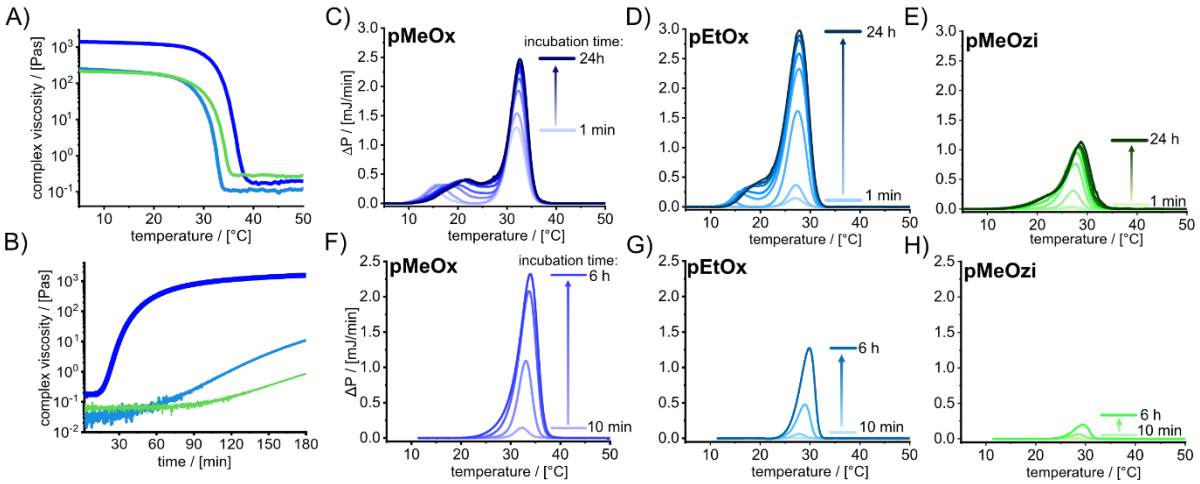

Figure 8| Modified ABA-type amphiphiles with varying hydrophilic A blocks and the aromatic pPheOzi B block and their thermogelation. A),B) Gel properties of 15 wt.% aqueous sol-gels of the polymers pMeOx-b-pPheOzi-b-pMeOx (dark blue), pEtOx-b-pPheOzi-b-pEtOx (light blue), pMeOzi-b-pPheOzi-b-pMeOzi (green). A) Temperature sweeps of the complex viscosity from 5-50 °C (heat rate: 0.05 °C). B) Gelation kinetics for 180 min. The gelation process was monitored at 5 °C by adding liquid samples at t=0 minutes. C)-H) Micro-DSC thermograms of 10 g/L solutions of C),F) pMeOx-*b*-pPheOzi-*b*-pMeOx, D),G) pEtOx-b-pPheOzi-b-pEtOx and E),H) pMeOzi-*b*-pPheOzi-*b*-pMeOzi. Solutions where held at 2 °C (C,D,E) and 10 °C (F,G,H) for time indicated prior to the thermoscan.

In aqueous solution, both novel polymers undergo inverse thermogelation (Figure 8 A,B and Figure S8) and form worm-like micelles in the cold as evidenced by TEM investigations (Figure S9). Dynamic light scattering at 5 and 40 °C confirmed a significant difference in self-assembly for all polymers (Figure S10, Table S4), similar as observed pMeOx-*b*-pPheOzi-*b*-pMeOx. Accordingly, the thermogelation again coincides with an order-order transition after exchanging the hydrophilic blocks.

However, significant differences in the complex viscosity at 5 °C (i.e. the gel strength), the T_{gel} upon heating (liquefaction temperature or gel persistence) and gelation kinetics (speed) were obtained in a temperature ramp experiment from 5 °C to 50 °C (polymer gels were stored at 5 °C for 48 h) and in a time sweep experiment for 180 minutes (pre-heated polymer solutions were transferred on a pre-cooled 5 °C plate and subsequently measured). In all three "disciplines" pMeOx-*b*-pPheOzi-*b*-pMeOx, showed the best performance. It exhibits an approximately 7-fold higher complex viscosity value at 5

°C compared to pEtOx-*b*-pPheOzi-*b*-pEtOx and pMeOzi-*b*-pPheOzi-*b*-pMeOzi. With respect to gel strength and persistence, only little differences were observed for the other two polymers. Only minutely higher gel strength (40 Pa*s) and slightly lower persistence (1-2 °C lower T_{gel}) was observed for the polymer pEtOx-*b*-pPheOzi-*b*-pEtOx in comparison to pMeOzi-*b*-pPheOzi-*b*-pMeOzi. In terms of gelation kinetics, pMeOx-*b*-pPheOzi-*b*-pMeOx undergoes a significant viscosity increase after 15 minutes. In contrast, the gelation kinetics of pEtOx-*b*-pPheOzi-*b*-pEtOx and pMeOzi-*b*-pPheOzi-*b*-pMeOzi are significantly delayed (approx. 5 to 8 times).

Finally, micro-DSC gives us an insight into the thermodynamics of the order-order transition in aqueous media. Thermograms were obtained after cooling to 2 °C or 10 °C for different time intervals (Figure 8 D-I). When hydrogels were incubated at 2 °C, the most prominent peak coincides for all three polymers with the sol-gel transition (Figure 8 D-F). The longer samples were cooled, the larger the signal, the maximum of which shifts to slightly larger temperature with longer incubation times. Interestingly, for both pMeOx-*b*-pPheOzi-*b*-pMeOx and pEtOx-*b*-pPheOzi-*b*-pEtOx, a smaller secondary peak starts at 10 °C – 13 °C and has a maximum at 15 °C after short incubation times, which shifts notably to higher temperature with longer incubation. This transition coincides with the step between 12 °C and 15 °C observed in the microviscosity (Figure 2 C,D). In comparison to pMeOx-*b*-pPheOzi-*b*-pMeOx, the transition at lower temperature is shifted to slightly higher temperatures in the case of pEtOx-*b*-pPheOzi-*b*-pEtOx while the larger transition at higher temperature is observed at lower temperatures, leading to a more pronounced overlap of both transitions. In the case of pMeOzi-*b*-pPheOzi-*b*-pMeOzi, only one major transition is observed upon liquefaction of the gel with only a shoulder (at 15-20 °C) emerging after cooling the sample 6 h or more. Interestingly, if the samples are cooled only to 10 °C instead of 2 °C, the secondary transitions at lower temperature are not observed at all (Figure 8 G-I). In addition while the height and integral of the main signal is attenuated by 20 % in the case of pMeOx-*b*-pPheOzi-*b*-pMeOx, the attenuation for both pEtOx-*b*-pPheOzi-*b*-pEtOx and pMeOzi-*b*-pPheOzi-*b*-pMeOzi is much more profound (70 % and 86 %, respectively).

This strong influence of the hydrophilic blocks on the gelation kinetics and thermodynamics as well as macroscopic gel properties clearly give a synthetic proof that the hydrophilic blocks play a crucial role in the gelation mechanism as shown before using a variety of advanced analytical tools. This mechanism described here is rather unusual, as the dehydration of (highly hydrophilic) MeOx units occurs in favor of inter- and intramolecular interaction with hydrophobic repeat units, which is unexpected. Also, this is clearly not simply a hydrophobic effect, as this would then be stronger for the less hydrophilic EtOx and MeOzi. We believe this discovery of a novel self-assembly mechanism opens up new possibilities to design stimulus responsive materials and will generally help to improve our understanding of the complex interactions of polymers in solutions.

Conclusion

Using a wide selection of complementary analytical tools, we gained a detailed picture of a novel and unusual order-order transition in conjunction with an inverse thermogelation of aqueous solutions of a special group of amphiphilic block copolymers. SAXS analysis confirmed the previously described reversible worm-to-sphere transition upon heating. WAXS experiments elucidated small changes during sol-gel transitions at 4-7 Å. Advanced NMR spectroscopic studies, supplemented by Raman and fluorescence spectroscopy at different temperatures revealed novel and unexpected polymer/polymer interactions between the hydrophilic pMeOx blocks and the hydrophobic aromatic pPheOzi moieties in the hydrogel state. Comparison with similar, tertiary amide containing systems in the literature and *in silico* molecular dynamics modeling led us to propose $n_{Am} \rightarrow \pi^*_{Ar}$ and/or $\pi_{Am} \bullet\bullet\bullet \pi_{Ar}$ interactions between the carbonyl moieties in the hydrophilic pMeOx block and the aromatic rings in the hydrophobic pPheOzi block to be responsible for the order-order transition and inverse thermogelation, likely in conjunction with more standard $\pi_{Ar} \bullet\bullet\bullet \pi_{Ar}$ hydrophobic interactions. To the best of our knowledge, the described system is the only example of a sphere-to-worm order-order transition that leads to inverse thermogelling, and it is also the first example in which non-ionic, non H-bonding interactions between the hydrophilic and hydrophobic compartment are critically affecting

the self-assembly in synthetic polymer amphiphiles. This mechanistic elucidation allowed us a tuning of this unusual system by changing the hydrophilic blocks leading to significant differences with respect to gel properties (strength and kinetics).

Notes

RL and HL are listed as inventors on a patent application pertinent to some materials in the present work. The other authors declare no competing financial interest.

Acknowledgment

The authors would like to gratefully acknowledge support by the Deutsche Forschungsgemeinschaft (DFG, German Research Foundation) – project number 326998133 – TRR 225 (subproject A03), awarded to R.L. and project number 440955393 awarded to A.-C.P. The authors thank Christian May for technical assistance and Bernhard Schummer for valuable discussions. We are very grateful for the HDRC-Software version 6.3.1 provided by O. Nirschl and K. Fischer, Physical Chemistry of Polymers at the Johannes Gutenberg University Mainz led by Prof. Dr. Sebastian Seiffert (formerly Prof. Dr. Manfred Schmidt) for DLS data analysis. Light scattering experiments were possible through support of the Deutsche Forschungsgemeinschaft (INST 93/774-1 FUGG). T.L. and E.S.L. acknowledge Academy of Finland for funding of the current research (Project Nos. 316893 and 323669). The authors are also grateful to Dr. Alexander Efimov for BPC12 synthesis. We gratefully acknowledge access to electron microscopy facilities provided by Prof. Bettina Böttcher at the Rudolf Virchow Center, Julius-Maximilians-University Würzburg. We also thank helpful discussions with Heikki Tenhu and the late Françoise Winnik.

References

1. Zhang, Q. L.; Weber, C.; Schubert, U. S.; Hoogenboom, R., Thermoresponsive polymers with lower critical solution temperature: from fundamental aspects and measuring techniques to recommended turbidimetry conditions. *Mater Horiz* **2017,** *4* (2), 109-116.
2. Seuring, J.; Agarwal, S., Polymers with Upper Critical Solution Temperature in Aqueous Solution. *Macromol Rapid Comm* **2012,** *33* (22), 1898-1920.
3. Niskanen, J.; Tenhu, H., How to manipulate the upper critical solution temperature (UCST)? *Polym Chem-Uk* **2017,** *8* (1), 220-232.
4. Lorson, T.; Jaksch, S.; Lübtow, M. M.; Jüngst, T.; Groll, J.; Lühmann, T.; Luxenhofer, R., A Thermogelling Supramolecular Hydrogel with Sponge-Like Morphology as a Cytocompatible Bioink. *Biomacromolecules* **2017,** *18* (7), 2161-2171.
5. Hoffman, A. S., Application of thermally reversible polymers and hydrogels in therapeutics and diagnostics. *Journal of Controlled Release* **1987,** *6*, 297-305.
6. Klouda, L.; Mikos, A. G., Thermoresponsive hydrogels in biomedical applications. *Eur J Pharm Biopharm* **2008,** *68* (1), 34-45.

7. Hecht, E.; Mortensen, K.; Hoffmann, H., L(3) Phase in a Binary Block Copolymer/Water System. *Macromolecules* **1995,** *28* (16), 5465-5476.
8. Blanazs, A.; Verber, R.; Mykhaylyk, O. O.; Ryan, A. J.; Heath, J. Z.; Douglas, C. W. I.; Armes, S. P., Sterilizable Gels from Thermoresponsive Block Copolymer Worms. *J Am Chem Soc* **2012,** *134* (23), 9741-9748.
9. Cunningham, V. J.; Ratcliffe, L. P. D.; Blanazs, A.; Warren, N. J.; Smith, A. J.; Mykhaylyk, O. O.; Armes, S. P., Tuning the critical gelation temperature of thermo-responsive diblock copolymer worm gels. *Polym Chem-Uk* **2014,** *5* (21), 6307-6317.
10. Penfold, N. J. W.; Lovett, J. R.; Verstraete, P.; Smets, J.; Armes, S. P., Stimulus-responsive non-ionic diblock copolymers: protonation of a tertiary amine end-group induces vesicle-to-worm or vesicle-to-sphere transitions. *Polym Chem-Uk* **2017,** *8* (1), 272-282.
11. Ratcliffe, L. P. D.; Derry, M. J.; Ianiro, A.; Tuinier, R.; Armes, S. P., A Single Thermoresponsive Diblock Copolymer Can Form Spheres, Worms or Vesicles in Aqueous Solution. *Angew Chem Int Edit* **2019,** *58* (52), 18964-18970.
12. Hahn, L.; Maier, M.; Stahlhut, P.; Beudert, M.; Flegler, V.; Forster, S.; Altmann, A.; Töppke, F.; Fischer, K.; Seiffert, S.; Böttcher, B.; Lühmann, T.; Luxenhofer, R., Inverse Thermogelation of Aqueous Triblock Copolymer Solutions into Macroporous Shear-Thinning 3D Printable Inks. *Acs Appl Mater Inter* **2020,** *12* (11), 12445-12456.
13. Haas, H. C.; Moreau, R. D.; Schuler, N. W., Synthetic Thermally Reversible Gel Systems .2. *J Polym Sci A2* **1967,** *5* (5pa2), 915-&.
14. Fu, W. X.; Zhao, B., Thermoreversible physically crosslinked hydrogels from UCST-type thermosensitive ABA linear triblock copolymers. *Polym Chem-Uk* **2016,** *7* (45), 6980-6991.
15. Fu, W. X.; Luo, C. H.; Morin, E. A.; He, W.; Li, Z. B.; Zhao, B., UCST-Type Thermosensitive Hairy Nanogels Synthesized by RAFT Polymerization-Induced Self-Assembly. *Acs Macro Lett* **2017,** *6* (2), 127-133.
16. Parmar, I. A.; Shedge, A. S.; Badiger, M. V.; Wadgaonkar, P. P.; Lele, A. K., Thermo-reversible sol-gel transition of aqueous solutions of patchy polymers. *Rsc Adv* **2017,** *7* (9), 5101-5110.
17. Witte, H.; Seeliger, W., Formation of Cyclic Imidic Esters by Reaction of Nitriles with Amino Alcohols. *Liebigs Ann Chem* **1974,** (6), 996-1009.
18. Hahn, L.; Lübtow, M. M.; Lorson, T.; Schmitt, F.; Appelt-Menzel, A.; Schobert, R.; Luxenhofer, R., Investigating the Influence of Aromatic Moieties on the Formulation of Hydrophobic Natural Products and Drugs in Poly(2-oxazoline)-Based Amphiphiles. *Biomacromolecules* **2018,** *19* (7), 3119-3128.
19. Dreiss, C. A.; Jack, K. S.; Parker, A. P., On the absolute calibration of bench-top small-angle X-ray scattering instruments: a comparison of different standard methods. *J Appl Crystallogr* **2006,** *39*, 32-38.
20. Zhang, F.; Ilavsky, J.; Long, G. G.; Quintana, J. P. G.; Allen, A. J.; Jemian, P. R., Glassy Carbon as an Absolute Intensity Calibration Standard for Small-Angle Scattering. *Metall Mater Trans A* **2010,** *41a* (5), 1151-1158.
21. Pauw, B. R.; Smith, A. J.; Snow, T.; Terrill, N. J.; Thunemann, A. F., The modular small-angle X-ray scattering data correction sequence. *J Appl Crystallogr* **2017,** *50*, 1800-1811.
22. Konefal, R.; Spevacek, J.; Cernoch, P., Thermoresponsive poly(2-oxazoline) homopolymers and copolymers in aqueous solutions studied by NMR spectroscopy and dynamic light scattering. *Eur Polym J* **2018,** *100*, 241-252.
23. Choe, C.; Lademann, J.; Darvin, M. E., Depth profiles of hydrogen bound water molecule types and their relation to lipid and protein interaction in the human stratum corneum in vivo. *Analyst* **2016,** *141* (22), 6329-6337.
24. Unal, M.; Akkus, O., Shortwave-infrared Raman spectroscopic classification of water fractions in articular cartilage ex vivo. *J Biomed Opt* **2018,** *23* (1).
25. Levitt, J. A.; Kuimova, M. K.; Yahioglu, G.; Chung, P. H.; Suhling, K.; Phillips, D., Membrane-Bound Molecular Rotors Measure Viscosity in Live Cells via Fluorescence Lifetime Imaging. *J Phys Chem C* **2009,** *113* (27), 11634-11642.

26. Lisitsyna, E.; Efimov, A.; Depresle, C.; Cauchois, P.; Vuorimaa-Laukkanen, E.; Laaksonen, T.; Durandin, N., Deciphering Multiple Critical Parameters of Polymeric Self-Assembly by Fluorescence Spectroscopy of a Single Molecular Rotor BODIPY-C12. *Macromolecules* **2021,** *54* (2), 655-664.
27. Bond, S. D.; Leimkuhler, B. J.; Laird, B. B., The Nosé-Poincaré method for constant temperature molecular dynamics. *J Comput Phys* **1999,** *151* (1), 114-134.
28. Sturgeon, J. B.; Laird, B. B., Symplectic algorithm for constant-pressure molecular dynamics using a Nose-Poincare thermostat. *J Chem Phys* **2000,** *112* (8), 3474-3482.
29. Maier, J. A.; Martinez, C.; Kasavajhala, K.; Wickstrom, L.; Hauser, K. E.; Simmerling, C., ff14SB: Improving the Accuracy of Protein Side Chain and Backbone Parameters from ff99SB. *J Chem Theory Comput* **2015,** *11* (8), 3696-3713.
30. Gerber, P. R.; Muller, K., Mab, a Generally Applicable Molecular-Force Field for Structure Modeling in Medicinal Chemistry. *J Comput Aid Mol Des* **1995,** *9* (3), 251-268.
31. Labute, P., The generalized Born/volume integral implicit solvent model: Estimation of the free energy of hydration using London dispersion instead of atomic surface area. *J Comput Chem* **2008,** *29* (10), 1693-1698.
32. *MOE. Molecular Operating Environment 2019.01.*, Chemical Computing Group ULC: 2019.
33. Yan, H.; Han, Z.; Li, K. M.; Li, G. Y.; Wei, X. L., Molecular Dynamics Simulation of the pH-Induced Structural Transitions in CTAB/NaSal Solution. *Langmuir* **2018,** *34* (1), 351-358.
34. Wang, Z. W.; Larson, R. G., Molecular Dynamics Simulations of Threadlike Cetyltrimethylammonium Chloride Micelles: Effects of Sodium Chloride and Sodium Salicylate Salts. *J Phys Chem B* **2009,** *113* (42), 13697-13710.
35. Wiest, J.; Kehrein, J.; Saedtler, M.; Schilling, K.; Cataldi, E.; Sotriffer, C. A.; Holzgrabe, U.; Rasmussen, T.; Bottcher, B.; Cronin-Golomb, M.; Lehmann, M.; Jung, N.; Windbergs, M.; Meinel, L., Controlling Supramolecular Structures of Drugs by Light. *Mol Pharmaceut* **2020,** *17* (12), 4704-4708.
36. Bayly, C. I.; Cieplak, P.; Cornell, W. D.; Kollman, P. A., A Well-Behaved Electrostatic Potential Based Method Using Charge Restraints for Deriving Atomic Charges - the Resp Model. *J Phys Chem-Us* **1993,** *97* (40), 10269-10280.
37. Frisch, M. J.; Trucks, G. W.; Schlegel, H. B.; Scuseria, G. E.; Robb, M. A.; Cheeseman, J. R.; Scalmani, G.; Barone, V.; Petersson, G. A.; Nakatsuji, H.; Li, X.; Caricato, M.; Marenich, A.; Bloino, J.; Janesko, B. G.; Gomperts, R.; Mennucci, B.; Hratchian, H. P.; Ortiz, J. V.; Izmaylov, A. F.; Sonnenberg, J. L.; Williams; Ding, F.; Lipparini, F.; Egidi, F.; Goings, J.; Peng, B.; Petrone, A.; Henderson, T.; Ranasinghe, D.; Zakrzewski, V. G.; Gao, J.; Rega, N.; Zheng, G.; Liang, W.; Hada, M.; Ehara, M.; Toyota, K.; Fukuda, R.; Hasegawa, J.; Ishida, M.; Nakajima, T.; Honda, Y.; Kitao, O.; Nakai, H.; Vreven, T.; Throssell, K.; Montgomery Jr., J. A.; Peralta, J. E.; Ogliaro, F.; Bearpark, M. J.; Heyd, J. J.; Brothers, E. N.; Kudin, K. N.; Staroverov, V. N.; Keith, T. A.; Kobayashi, R.; Normand, J.; Raghavachari, K.; Rendell, A. P.; Burant, J. C.; Iyengar, S. S.; Tomasi, J.; Cossi, M.; Millam, J. M.; Klene, M.; Adamo, C.; Cammi, R.; Ochterski, J. W.; Martin, R. L.; Morokuma, K.; Farkas, O.; Foresman, J. B.; Fox, D. J. *Gaussian 16 Rev. C.01*, 2016.
38. Wang, J. M.; Wolf, R. M.; Caldwell, J. W.; Kollman, P. A.; Case, D. A., Development and testing of a general amber force field. *J Comput Chem* **2004,** *25* (9), 1157-1174.
39. Case, D. A.; Cheatham, T. E.; Darden, T.; Gohlke, H.; Luo, R.; Merz, K. M.; Onufriev, A.; Simmerling, C.; Wang, B.; Woods, R. J., The Amber biomolecular simulation programs. *J Comput Chem* **2005,** *26* (16), 1668-1688.
40. Jorgensen, W. L.; Chandrasekhar, J.; Madura, J. D.; Impey, R. W.; Klein, M. L., Comparison of Simple Potential Functions for Simulating Liquid Water. *J Chem Phys* **1983,** *79* (2), 926-935.
41. Phillips, J. C.; Braun, R.; Wang, W.; Gumbart, J.; Tajkhorshid, E.; Villa, E.; Chipot, C.; Skeel, R. D.; Kale, L.; Schulten, K., Scalable molecular dynamics with NAMD. *J Comput Chem* **2005,** *26* (16), 1781-1802.
42. Darden, T.; York, D.; Pedersen, L., Particle Mesh Ewald - an N.Log(N) Method for Ewald Sums in Large Systems. *J Chem Phys* **1993,** *98* (12), 10089-10092.
43. Roe, D. R.; Cheatham, T. E., PTRAJ and CPPTRAJ: Software for Processing and Analysis of Molecular Dynamics Trajectory Data. *J Chem Theory Comput* **2013,** *9* (7), 3084-3095.

44. Humphrey, W.; Dalke, A.; Schulten, K., VMD: Visual molecular dynamics. *J Mol Graph Model* **1996,** *14* (1), 33-38.
45. *The PyMOL Molecular Graphics System*, Version 2.4.1; Schrödinger LLC.
46. Renouprez, A. J., *Catalyst Characterization: Physical Techniques for Solid Materials*. Springer US: Boston, MA, USA, 1994.
47. Hyland, L. L.; Taraban, M. B.; Yu, Y. B., Using small-angle scattering techniques to understand mechanical properties of biopolymer-based biomaterials. *Soft Matter* **2013,** *9* (43), 10218-10228.
48. Baral, A.; Basak, S.; Basu, K.; Dehsorkhi, A.; Hamley, I. W.; Banerjee, A., Time-dependent gel to gel transformation of a peptide based supramolecular gelator. *Soft Matter* **2015,** *11* (24), 4944-4951.
49. Kruszynski, R.; Sieranski, T., Can Stacking Interactions Exist Beyond the Commonly Accepted Limits? *Cryst Growth Des* **2016,** *16* (2), 587-595.
50. Wei, L. F.; Zhang, W. B.; Ma, J. Z.; Bai, S. L.; Ren, Y. J.; Liu, C.; Simion, D.; Qin, J. B., pi-pi stacking interface design for improving the strength and electromagnetic interference shielding of ultrathin and flexible water-borne polymer/sulfonated graphene composites. *Carbon* **2019,** *149*, 679-692.
51. Boireau-Adamezyk, E.; Baillet-Guffroy, A.; Stamatas, G. N., Mobility of Water Molecules in the Stratum Corneum: Effects of Age and Chronic Exposure to the Environment. *J Invest Dermatol* **2014,** *134* (7), 2046-2049.
52. Vyumvuhore, R.; Tfayli, A.; Duplan, H.; Delalleau, A.; Manfait, M.; Baillet-Guffroy, A., Effects of atmospheric relative humidity on Stratum Corneum structure at the molecular level: ex vivo Raman spectroscopy analysis. *Analyst* **2013,** *138* (14), 4103-4111.
53. Dent, M. R.; Lopez-Duarte, I.; Dickson, C. J.; Geoghegan, N. D.; Cooper, J. M.; Gould, I. R.; Krams, R.; Bull, J. A.; Brooks, N. J.; Kuimova, M. K., Imaging phase separation in model lipid membranes through the use of BODIPY based molecular rotors. *Phys Chem Chem Phys* **2015,** *17* (28), 18393-18402.
54. Vysniauskas, A.; Lopez-Duarte, I.; Duchemin, N.; Vu, T. T.; Wu, Y. L.; Budynina, E. M.; Volkova, Y. A.; Cabrera, E. P.; Ramirez-Ornelas, D. E.; Kuimova, M. K., Exploring viscosity, polarity and temperature sensitivity of BODIPY-based molecular rotors. *Phys Chem Chem Phys* **2017,** *19* (37), 25252-25259.
55. Hiller, W.; Engelhardt, N.; Kampmann, A. L.; Degen, P.; Weberskirch, R., Micellization and Mobility of Amphiphilic Poly(2-oxazoline) Based Block Copolymers Characterized by 1-H NMR Spectroscopy. *Macromolecules* **2015,** *48* (12), 4032-4045.
56. Brown, S. P., Advanced solid-state NMR methods for characterising structure and self-assembly in supramolecular chemistry, polymers and hydrogels. *Curr Opin Colloid In* **2018,** *33*, 86-98.
57. Newberry, R. W.; Raines, R. T., The n ->pi* Interaction. *Accounts Chem Res* **2017,** *50* (8), 1838-1846.
58. Gorske, B. C.; Bastian, B. L.; Geske, G. D.; Blackwell, H. E., Local and tunable n ->pi* interactions regulate amide isomerism in the peptoid backbone. *J Am Chem Soc* **2007,** *129* (29), 8928.
59. Thurn, H.; Hoffmann, H., Evidence of Sticky Contacts between Wormlike Micelles in Viscoelastic Surfactant Solutions. *Langmuir* **2019,** *35* (37), 12192-12204.
60. Egli, M.; Sarkhel, S., Lone pair-aromatic interactions: To stabilize or not to stabilize. *Accounts Chem Res* **2007,** *40* (3), 197-205.
61. Hahn, L.; Kessler, L.; Polzin, L.; Fritze, L.; Forster, S.; Helten, H.; Luxenhofer, R., ABA Type Amphiphiles with Poly(2-benzhydryl-2-oxazine) Moieties: Synthesis, Characterization and Inverse Thermogelation. *Macromol Chem Phys* **2021**.
62. Hahn, L.; Karakaya, E.; Zorn, T.; Sochor, B.; Maier, M.; Stahlhut, P.; Forster, S.; Fischer, K.; Seiffert, S.; Poppler, A. C.; Detsch, R.; Luxenhofer, R., An Inverse Thermogelling Bioink Based on an ABA-Type Poly(2-oxazoline) Amphiphile. *Biomacromolecules* **2021,** *22* (7), 3017-3027.